

# Measurements of the Flowfield Interaction Between Tandem Cylinders

Dan H. Neuhart<sup>\*</sup>, Luther N. Jenkins<sup>\*</sup>, Meelan M. Choudhari<sup>†</sup>, and Mehdi R. Khorrami<sup>†</sup>  
*NASA Langley Research Center, Hampton, Virginia, 23681*

This paper presents the most recent measurements from an ongoing investigation of the unsteady wake interference between a pair of circular cylinders in tandem. The purpose of this investigation is to help build an in-depth experimental database for this canonical flow configuration that embodies the effects of component interaction in landing gear noise. This new set of measurements augments the previous database at the primary Reynolds number (based on tunnel speed and cylinder diameter) of  $1.66 \times 10^5$  in four important respects. First, better circumferential resolution of surface pressure fluctuations is obtained via cylinder “clocking”. Second, higher resolution particle image velocimetry measurements of the shear layer separating from the cylinders are achieved. Third, the effects of simultaneous boundary layer trips along both the front and rear cylinders, versus front cylinder alone in the previous measurements, are studied. Lastly, on-surface and off-surface characteristics of unsteady flow near the “critical” cylinder spacing, wherein the flow switches intermittently between two states that are characteristic of lower and higher spacings, are examined. This critical spacing occurs in the middle of a relatively sudden change in the drag of either cylinder and is characterized by a loud intermittent noise and a flow behavior that randomly transitions between shear layer attachment to the rear cylinder and constant shedding and rollup in front of it. Analysis of this bistable flow state reveals much larger spanwise correlation lengths of surface pressure fluctuations than those at larger and smaller values of the cylinder spacing.

## Nomenclature

$D$	= cylinder diameter
$c_d$	= sectional drag coefficient
$C_p$	= pressure coefficient, $\frac{p - p_\infty}{q_\infty}$
$C_p'_{rms}$	= fluctuating pressure coefficient, $\frac{p'_{rms}}{q_\infty}$
$G_{xx}$	= one-sided power spectral density for variable $x$
$L_{corr}/D$	= nondimensional, longitudinal correlation length, $\int_0^\infty R_{pp} d(\Delta z / D)$
$p'_{rms}$	= root-mean-square pressure fluctuation
$p$	= instantaneous pressure measured on model surface
$p_\infty$	= free-stream static pressure
$q_\infty$	= free-stream dynamic pressure
$R_{pp}$	= cross correlation coefficient of pressure fluctuations
$L$	= distance between cylinder centers
TKE	= turbulent kinetic energy, $\frac{1}{2}((u'_{rms})^2 + (v'_{rms})^2)$

<sup>\*</sup> Research Engineer, Flow Physics and Control Branch

<sup>†</sup> Research Engineer, Computational AeroSciences Branch, Associate Fellow, AIAA

$u'_{\text{rms}}$	=	root-mean-square streamwise velocity fluctuation
$v'_{\text{rms}}$	=	root-mean-square lateral velocity fluctuation
$X$	=	streamwise coordinate
$Y$	=	vertical coordinate
$\Delta z$	=	spanwise distance between unsteady pressure sensors
$\theta$	=	azimuthal position relative to cylinder axis

## I. Introduction

Along with high-lift devices, the landing gear of aircraft are known to be an important source of noise during approach conditions<sup>1,2</sup>. However, the complexity of the landing gear geometry and the resulting unsteady flow field in the vicinity of the gear poses severe challenges to the development and application of physics based models for landing gear noise. In an effort to increase the understanding of noise generation mechanisms and to help develop high fidelity noise prediction methods for landing gear systems, researchers at NASA have been conducting experiments on a set of simpler geometries that highlight the pertinent features of the landing gear flow field. The tandem cylinder arrangement provides one such canonical geometry, which produces the type of unsteady flow interaction commonly associated with landing gear components, namely, the wake from an upstream bluff body interacting with a downstream body. The current tandem cylinder configuration has previously been tested in both the Basic Aerodynamics Research Tunnel (BART)<sup>2,3</sup> and the Quiet Flow Facility (QFF)<sup>4-6</sup> at NASA Langley Research Center (LaRC). Accompanying computations of both near-field unsteadiness and noise radiation have been reported in Refs. 5-8.

Due to the applicability of tandem cylinder arrangements to other endeavors, such as cooling, venting, and structural support, numerous additional studies of tandem cylinder arrangements have been reported in the literature. The comprehensive review by Zdravkovich<sup>9</sup> outlines the multiple flow patterns associated with different separation distances ( $L/D$ ) between the cylinders. At effectively subcritical Reynolds numbers (such that the boundary layer along the cylinder surface remains laminar at the location of separation) and separation distances of  $2.5 < L/D < 3.2$ , intermittent vortex shedding can be detected in the gap region between the cylinders and vortex shedding occurs behind the rear cylinder. The intermittent nature of the flow is characterized by periods of separated shear layer reattachment on the forward face of the rear cylinder and rollup of the shear layer into distinct, shed vortices. For  $3.2 < L/D < 3.8$ , the flow between the cylinders is bistable and switches between intermittent shedding and constant shedding. A similar bistable state also occurs at effectively higher, i.e., post-critical Reynolds numbers, such that the cylinder boundary layer becomes turbulent prior to separation. However, the associated flow characteristics within the higher Reynolds number regime have not been investigated in detail and constitute one of the primary issues addressed in this study.

To simulate the tandem cylinder flow-field at post-critical Reynolds numbers, Jenkins, et al.<sup>2,3</sup> tripped the boundary layer along the front cylinder ahead of flow separation. Particle Image Velocimetry (PIV), static surface pressure, and limited hot wire measurements were obtained over a range of cylinder spacings to help validate numerical simulations of the near-field flow behavior. To acquire a more comprehensive dataset for the validation of aeroacoustic predictions, including unsteady surface pressures and the radiated acoustic field, a second model was fabricated and tested in the BART<sup>3</sup> and QFF<sup>5,6</sup> facilities. The purpose of the present paper is to extend the previous documentation of the steady and unsteady surface pressures and off-body flow field in several important respects. In particular, our goal is to provide a) better circumferential resolution of the surface pressure fluctuations, b) insight into the state of the shear layer just downstream of boundary-layer separation from the cylinder surfaces, c) data on the effect of a trip on the rear cylinder, d) a deeper understanding of the flow field within the bistable state, and e) a complementary dataset at other  $L/D$  separations. We note that the bistable state case poses major challenges for numerical simulations due to sensitivity of the flow behavior and the long integration times required to gather reliable statistical information; therefore, experimental measurements are particularly valuable to guide the numerical simulations within this regime.

## II. Experimental Apparatus and Techniques

### A. Test Facility

The experiment was conducted in the BART facility at NASA LaRC. This tunnel is a subsonic, atmospheric wind tunnel used to investigate the fundamental characteristics of complex flow fields and to acquire detailed data for the development and validation of computational fluid dynamics (CFD) models and methods. The tunnel has a closed test section with a height of 28 inches (0.711 m), a width of 40 inches (1.016 m), and a length of 120 inches (3.048 m). The free stream velocity was set to 144 ft/s (44 m/s) to achieve a Reynolds number based on cylinder diameter of  $1.66 \times 10^5$ , corresponding to the primary Reynolds number for the measurements in Refs. 2 and 3. At these conditions, the free stream turbulence level is less than 0.10%. Additional information about the BART can be found in Refs. 10 and 11.

### B. Model

The tandem cylinder arrangement used in the present study is shown in the photograph in Fig. 1 and the schematic drawing of Fig. 2. Whereas the first set of tests in Ref. 2 employed a tandem cylinder model with 1.75 inch (44.45 mm) diameter cylinders mounted vertically within the test section, both Ref. 3 and the current experiment utilized a model with 2.25 inch (57.15 mm) diameter cylinders, also mounted vertically. Each cylinder was attached to a base that was inserted into a track mechanism secured to the tunnel floor. With this arrangement, the front cylinder was fixed and the rear cylinder could be translated upstream and downstream to achieve the desired spacing. As described in Ref. 3, the models were instrumented with circumferential (red arrows, Fig. 1) and axial distributions of static pressure orifices and piezoresistive differential pressure transducers (beneath a surface pinhole) for measuring the steady and fluctuating pressures, respectively. The installed pressure transducers were 2-psi differential, piezoresistive sensors.

To produce a turbulent boundary layer and achieve the type of flow separation associated with post-critical Reynolds numbers, serrated transition strips were attached along the entire span of the upstream cylinder in the regions between  $\theta = 50^\circ$  and  $\theta = 60^\circ$  and between  $\theta = 300^\circ$  and  $\theta = 310^\circ$ . The effectiveness of the transition strip in producing a post-critical type flow was established by the good agreement between mean  $C_p$  distributions for a single cylinder from both models (from Refs. 2 and 3) and the data from Roshko<sup>12</sup> at a Reynolds number of  $8.6 \times 10^6$ .

### C. Measurement Techniques and Error Analysis

The measurement techniques used in this study were a combination of the techniques used in the previous two BART entries<sup>2,3</sup>. Analysis of the PIV data provided detailed insight into the steady and unsteady near-field flow structure. The procedure used to acquire and process the PIV data is described in Ref. 2. Steady and unsteady pressures were simultaneously measured on the front and rear cylinders using the static orifices and transducers mentioned in the previous section. Reference 3 contains a description of the procedure used to acquire and process the steady and unsteady pressure data and also contains estimates of uncertainties in various measurements and convergence indicators for statistical information derived from those measurements. Estimates of experimental uncertainties are given in Table 1. Most absolute values are given based on nominal tunnel conditions or on an average data value. Percentage values are quoted for parameters where the uncertainty equations were posed in terms of the uncertainty relative to the nominal value of the parameter. Specifications of the PIV system are given in Table 2.

## III. Results and Discussion

A critical first step during the experimental campaign reported in this paper was to establish consistency between the present and previous measurements in the BART facility. This is particularly important to help achieve the goal of an accurate yet robust dataset that is suitable for the benchmarking of CFD computations. In Jenkins, et al.<sup>3</sup>, consistency between the first two entries involving two separate models was established by comparing mean surface pressure distributions and the integrated lift and drag coefficients at representative cylinder spacings. Following this approach for the current experiment, the steady surface pressure measurements for an L/D of 3.7 proved to be

almost identical to those from the same diameter model in the previous test entry<sup>3</sup>. However, for an  $L/D$  of 1.435, where asymmetric pressures along the rear cylinder cannot be avoided, the observed asymmetry during the current entry was found to be opposite (but otherwise similar) to that in the prior entry (Fig. 3). The latter change in asymmetric behavior has a negligible effect on the overall drag coefficient at this spacing as evidenced in Fig. 4, which shows the pressure drag based on integration of steady  $C_p$  as a function of the cylinder spacing. Comparable streamlines from PIV measurements during the previous and current tests are shown in Figs. 5a and 5b, respectively. Clearly, the flow patterns in Figs. 5a and 5b closely resemble each other, except for the reversal of the pattern with respect to the direction of the free-stream flow (i.e.,  $x$ -axis). The data discussed here and in sections A and B that follow were taken with the boundary layer on the rear cylinder untripped. The effects of tripping the boundary layer on the rear cylinder will be examined in section C.

#### A. Bistable Flow State

As may also be noted in the drag plot of Fig. 4, there is a region of relatively sudden “drag rise” near  $L/D=3$ . This drag rise has been described in many references<sup>13-17</sup>, and the  $L/D$  of its onset varies across the experiments. As stated above, the cylinder spacings in the vicinity of this rapid rise correspond to a bistable state wherein the flow randomly switches between constant shedding and intermittent shedding in the gap region between the two cylinders. Frequency spectra do not easily reveal the bistable character of the flow because of the randomness of the switching, representing a non-stationary, non-periodic flow. A conventional calculation of the frequency spectra assumes stationarity, so that the intermittent, time-dependent nature of the bistable flow is lost during such calculations. This point is illustrated in Fig. 6 which compares the power spectral density (PSD) curves at  $L/D=1.435$ , 3.0375 (middle of the drag rise), and 3.7, for the unsteady pressure transducer on the rear cylinder at the  $\theta = 45^\circ$  location (indicated by red arrow in Fig. 6). The spectrum for  $L/D = 3.0375$  only shows the constant shedding mode. The intermittent nature of the flow in the middle of the drag rise is, however, obvious from the spectrograms of the signals in Fig. 7. A spectrogram, or short-time Fourier transform (STFT)<sup>18,19</sup>, allows one to look at a time-varying spectrum, i.e., it shows the time-dependent behavior of the spectra. For the same transducer location as in Fig. 6, the spectrogram for  $L/D=3.7$  (constant shedding) is shown in Fig. 7a, and that for  $L/D=3.0375$  (intermittent shedding) in Fig. 7b. In these plots, the frequency resolution (i.e., resolution along the vertical axis) in the spectrograms is 3.125 Hz, and the time resolution (i.e., resolution along the horizontal axis) is 0.16 sec. The highest amplitudes are displayed in red, and decrease in order through orange, yellow and green. The amplitude values are calculated in decibels, i.e., as 10 times the common log of the single-sided PSD. Tonal peaks are represented by horizontal lines. In Fig. 7a, for the  $L/D=3.7$  case, the dominant spectral peak corresponds to a distinct horizontal line, indicating the presence of continuous periodic shedding at a frequency of about 181 Hz. The time series for the pressure signal is shown in the inset and reveals a relatively constant maximum amplitude. In Fig. 7b for  $L/D=3.0375$ , the tonal peak at approximately 168 Hz is not constant, but is randomly interrupted along the time axis, indicating a nonstationary flow. This spectrogram behavior is consistent with the intermittent audible noise that was heard during the test when the bistable state existed. The signal shown in the inset reveals an intermittent reduction in the maximum signal amplitude when the tonal peak line in the spectrogram either disappears or weakens considerably.

Fig. 7c shows the expanded time series of the pressure signal for  $L/D=3.7$ , indicating a clearly periodic flow. The time series in Fig. 7d shows a similarly periodic signal, with a slightly longer period, for the periodic portion of the time series for  $L/D=3.0375$ . The expanded time series for the aperiodic portion of the signal for  $L/D=3.0375$  is shown in Fig. 7e. Clearly, the signal displays a random behavior and a reduced amplitude.

An alternate way to look at the effect of the bistable state is to calculate the spanwise cross-correlation between sensors at a given azimuthal angle on the cylinders. These correlation curves can then be integrated (Ref. 20) to yield the appropriate correlation length scales, indicating the spatial extent over which the signals remain correlated. More importantly, the correlation lengths indicate the extent of the wake’s two-dimensionality along the cylinder axis and the relative distance downstream over which shedding continues (since longer correlations lengths mean that shedding propagates farther downstream<sup>21</sup>). The correlation data provides useful guidance to CFD researchers regarding the required spanwise extent of their computational domain for adequate simulation of the noise sources. For instance, a higher correlation length implies the need for a correspondingly broader spanwise domain for numerical simulations, especially when the main objective involves acoustic predictions.

As a first step in extracting the spanwise correlation length, the cross-correlation coefficients of measured unsteady pressures along a constant  $\theta$  line were calculated and the results for  $\theta = 135^\circ$  along the aft cylinder are

plotted in Fig. 8a. For  $L/D=1.435$ , the correlation coefficients drop steeply as the distance between sensors increases, depicting relatively small correlation lengths. This is indicative of a large level of three-dimensionality, as evidenced in previous studies by a high level of spanwise flow aft of separation<sup>3</sup>. For  $L/D=3.7$ , the correlation coefficients remain relatively high for much larger sensor spacings, indicating longer correlation lengths at supercritical spacing. For  $L/D=3.0375$ , the correlation coefficients are higher than for  $L/D=3.7$ ; however, there is considerable spread in the data, as would be expected for this bistable condition, since the flow is switching between shedding and non-shedding modes. Also of note is that the correlation does not go to zero for this case at the largest sensor spacing, 7 diameters.

To obtain an overall picture of how the spanwise correlations varied with cylinder spacing, the integral correlation length for sensors at  $\theta = 135^\circ$  has been plotted versus  $L/D$  in Fig. 8b. A cubic spline fit of the correlation coefficient curves was used to evaluate the area under the correlation function, yielding the correlation length. In cases where the correlation curve dropped below zero, the integration was cut off at that point<sup>20</sup>. Conversely, when the curve remained positive beyond the maximum sensor spacing of 7 diameters, as in the bistable state, it was only integrated out to that value. For those cases, the actual correlation lengths would be longer than the values indicated in Fig. 8b and, in some cases, significantly so. However, integrating the curves up to zero correlation coefficient would have required extrapolating the curve beyond the range of the existing data, which we elected not to do.

The significantly higher correlation lengths along both front and rear cylinders within the bistable state indicate the possibility of potentially higher acoustic levels within this narrow range of cylinder spacing, provided that the amplitudes of the surface pressure fluctuation remain comparable to those just outside of this critical regime. Accompanying tests in QFF will help determine whether or not the acoustic levels are indeed higher at the critical spacing as well as establish the sensitivity of the bistable flow characteristics to tunnel disturbances. It is worth mentioning that an intermittent but loud noise was heard in the BART control room during the  $L/D = 3.0375$  runs, which was probably associated with the intervals when the bistable state was in the tonal mode. Because the tonal peak of 168 Hz happens to be rather close to the frequency of an oblique duct mode (mode (1,0) based on the tunnel cross-sectional dimensions of 40 inches), a resonance between the shedding mode and the duct acoustic mode may have contributed to the increased intensity of the acoustic radiation transmitted outside of the tunnel walls.

The strength of the acoustic field radiating from the tandem cylinder configuration is also related to the RMS level of the local unsteady lift (which is a function of the RMS of pressure fluctuations). The RMS of pressure fluctuations along the rear cylinder are presented in coefficient form in Fig. 9 for each of the three  $L/D$  cases from Fig. 6. The red arrows point to the original azimuthal angles of the installed sensors around the circumference of the cylinder. The remaining data points were obtained by rotating the model in  $5^\circ$  increments in the azimuthal direction. Clearly, this “clocking” action has allowed us to resolve the details in the azimuthal distribution of  $Cp'_{rms}$  that would not have been possible otherwise. Just as the standard power spectral density calculations do not properly depict the bistable flowfield, the RMS pressures shown in Fig. 9 do not give any evidence of the intermittent nature of the bistable state for  $L/D=3.0375$ , nor does the value reflect either state. In fact, the only way the rms will have any meaning is if the bistable data are conditionally sampled. Note, the highest pressure fluctuation levels along the rear cylinder are observed near azimuthal angles where the shear layers from the upstream cylinder typically reattach ( $\theta = 40^\circ$  to  $60^\circ$  on either side of  $0^\circ$ ). Therefore, the sensor at  $\theta = 45^\circ$  will be used later to examine the unsteady flow characteristics in more detail.

The intermittent nature of the bistable state can be further investigated by examining the contours of instantaneous velocity and vorticity fields as derived from the PIV data. Figures 10 and 11 display two representative sets of selected images of the flow field just ahead of the rear cylinder, within the gap between the cylinders, at  $L/D=3.0375$ . The contour plots in Fig. 10 indicate a flow mode where both upper and lower shear layers may be simultaneously attached to the rear cylinder. At the same  $L/D$ , Fig. 11 shows the other bistable mode, wherein the shear layers roll up in front of the rear cylinder. Similar qualitative results were found using smoke flow visualization by Igarashi<sup>15</sup>.

An additional characteristic of the bistable flow state is shown by the probability density function (PDF) estimates of unsteady surface pressure in Fig. 12. These figures show the estimated probability of occurrence of the instantaneous pressures measured by the transducer at  $\theta = 45^\circ$  on the rear cylinder. For  $L/D=1.435$  (Fig. 12a), where no shedding was observed in the PIV data, a single central peak appears in the distribution for the recirculating flow that existed near the sensor location. For  $L/D=3.7$ , Fig. 12b shows a bimodal distribution of the unsteady pressure at

the same sensor location, indicating the presence of alternate vortex shedding from the top and bottom sides of the cylinder. Lastly, the PDF in Fig. 12c, for  $L/D=3.0375$ , reveals a distribution that appears to combine the features of PDFs at subcritical and supercritical spacings. With simultaneously attached shear layers, the single peak distribution would exist, whereas with vortex shedding in front of the sensor, the outer (bimodal) peaks would be manifested.

### ***B. Shear Layer Separating from Cylinder Surfaces***

PIV measurements of Ref. 2 provided a satisfactory global picture of the tandem cylinder flow field. However, such a large field of view necessarily under-resolves critical flow features such as flow separation from the cylinder surface and the local dynamics of the separated shear layer. An important goal of the present study was to remedy this shortcoming by confining the available resolution to a smaller field of view. Contours of instantaneous spanwise vorticity in the separated flow region between the cylinders for  $L/D=1.435$ , at the higher PIV resolution (0.649 mm), are shown in Fig. 13. Two frames chosen from the ensemble of acquired images show the separated shear layer from the front cylinder impinging on the rear cylinder. In Fig. 13a, the shear layer appears relatively horizontal, and in Fig. 13b, it has meandered up slightly. This gives visual evidence of what may be one of the causes of the broadband “humps” in some of the pressure spectra in the attachment region. In Ref. 3, it was speculated that the broadband character could be due to shear layer meandering and/or the vortical structures of various scales being convected across the sensor orifice in the attachment region.

For  $L/D=3.7$ , instantaneous spanwise vorticity is shown for the separated shear layer from the back side of the front cylinder in Fig. 14. In Fig. 14a, a larger rollup of the layer has commenced, and in Fig. 14b, a smaller rollup is in progress. Fig. 15 shows instantaneous views of the flow separating from the rear cylinder for  $L/D=3.7$ , and two extremes of the fluctuating separation location are in evidence. In Fig. 15a, the separation point is further along the cylinder surface than in Fig 15b and the free shear layer is rolling up close to the surface directly behind the cylinder (in the interior of the wake). In Fig. 15b, the flow separates from the cylinder surface further upstream than in Fig 15a and the shear layer deflects out towards the wake exterior away from the cylinder surface. These variations of flow were not uncommon in the ensemble of instantaneous PIV data frames. The fluctuating separation location in conjunction with the azimuthal pressure gradient just ahead of the instantaneous separation location (Fig. 9, peaks around  $110^\circ$  and  $250^\circ$ ) likely accounts for the elevated levels of the RMS pressures at these locations, .

### ***C. Unsteady Surface Pressures and Effects of Boundary Layer Tripping Along Rear Cylinder***

All of the measurements described thus far (as well as those reported in the earlier papers based on the same model<sup>2,3</sup>) were obtained without any trip on the rear cylinder. Because of the impingement of the turbulent wake from the upstream cylinder, it might be expected that the boundary layer flow just ahead of separation from the rear cylinder is also turbulent or, at least, highly disturbed. As an alternative to the difficult task of detecting the state of the boundary layer upstream of separation, similar measurements were repeated after mounting a trip on the rear cylinder in addition to the trip already placed along the front cylinder. The effect of the rear-cylinder trip on time averaged surface pressures along both cylinders is shown in Fig. 16. The pressure distributions for  $L/D=1.435$  in Fig. 16a show that the rear cylinder trip has a negligible effect on the pressure distribution along the front cylinder (although not shown, this is true for  $L/D=3.7$  as well). The effect on the rear cylinder for this subcritical spacing is also negligible, except for a slight difference in the negative pressure peak near  $\theta=270^\circ$ . For  $L/D=3.7$  (Fig. 16b), however, the rear cylinder trip can have a significant effect on the pressure distribution along the downstream cylinder depending on the azimuthal location of the trip. The highest negative pressure peaks occur for the untripped rear cylinder. As the trip is moved aft circumferentially, the magnitudes of these peaks are progressively reduced. The difference in the peak values between the  $60\text{-}70^\circ$  trips and the  $70\text{-}80^\circ$  trips are quite small, indicating a lack of sensitivity to the trip location within this range.

The pressure distribution for the untripped rear cylinder shows that boundary layer separation occurs between  $120^\circ$  and  $130^\circ$  and that the highest level of pressure recovery is observed for this configuration. Integration of the mean pressures reveals that it also has the lowest drag coefficient. The remaining distributions indicate an earlier boundary layer separation at  $120^\circ$  in the presence of the rear cylinder trip, with progressively less pressure recovery as the trip location moves from between  $50^\circ\text{-}60^\circ$  to between  $70^\circ\text{-}80^\circ$ . The drag coefficients calculated for the  $60^\circ\text{-}70^\circ$  trips and the  $70^\circ\text{-}80^\circ$  trips are nearly equal, but higher than those for the  $50^\circ\text{-}60^\circ$  trips.

Since the effect of tripping the boundary layer on the rear cylinder (at  $70^\circ$ - $80^\circ$ ) was manifested primarily on the rear cylinder for  $L/D=3.7$ , close-up views of mean spanwise vorticity were examined from the PIV data for this case and the results are displayed in Fig. 17. For comparison purposes, both untripped (Fig.17a) and tripped (Fig.17b) flows behind the rear cylinder are shown. (Note that the boundary layer along the front cylinder is tripped in both cases.) Although no significant difference is seen in the respective levels of vorticity, the region of high vorticity appears to lie somewhat closer to the cylinder in the untripped case, which is consistent with the comparison of the mean surface pressure distributions (Fig. 16b) that separation is delayed when the rear cylinder was untripped, so the flow remains attached for a longer distance around the cylinder. The corresponding distributions of turbulent kinetic energy, TKE, are shown in Figs. 18a and 18b for untripped and tripped flows, respectively. In this case, the TKE levels in the vicinity of the mean separation location are higher for the untripped case, showing more energy being injected into the wake via the separated shear layer. Both the higher TKE as well as the delayed mean separation in the untripped case might be attributed to the highly transitional nature of the approaching boundary layer.

Similar to the mean surface pressures, the effect of tripping the rear cylinder at  $L/D=3.7$  on the distribution of RMS pressure coefficient was manifested primarily at the peaks (Fig. 19). In this case, the peak  $Cp'_{rms}$  values at around  $110^\circ$  and  $240^\circ$  (separation areas) and, to a lesser extent, those near  $45^\circ$  and  $315^\circ$  (reattachment areas) exhibit the largest impact due to boundary-layer tripping on the rear cylinder. Clocked data were taken only for the untripped and the  $70^\circ$ - $80^\circ$  trip configurations and, hence, those are the only two cases that capture the peak in  $Cp'_{rms}$  distribution near the separation locations. It should be mentioned that we had to reapply the trip when clocking the cylinders to maintain a constant azimuthal trip location. Consistent with the highly energized nature of the (presumably) transitional boundary layer in the untripped case, that case shows the higher values of peak  $Cp'_{rms}$  near the  $110^\circ$  and  $240^\circ$  azimuthal locations. In the vicinity of the reattachment location ( $\theta = \pm 45^\circ$ ), the highest values of peak  $Cp'_{rms}$  occurred for the untripped case, as well, followed by the  $60^\circ$ - $70^\circ$  trips and the  $70^\circ$ - $80^\circ$  trips. The  $50^\circ$ - $60^\circ$  trips showed the lowest peak levels; however, the measurements at  $\theta = \pm 45^\circ$  are very likely to have been influenced by the proximity to the  $50^\circ$ - $60^\circ$  trip. The effect of the trips on the spectra in the separation area on the rear cylinder (Fig. 20) is manifested as a broadband decrease in the level of the PSD (except at the tonal peak) in the tripped case. This is again consistent with the reduced level of TKE in Fig. 18b for the tripped flow.

Spanwise coherence (coherence as function of sensor spacing at a given frequency) can give insight into spanwise uniformity in the flow. The distribution of spanwise coherence, at an azimuthal angle of  $135^\circ$  on the rear cylinder, showed no significant difference between the tripped and untripped rear cylinder configurations at the peak shedding frequency for  $L/D=3.7$ . The spanwise coherence data for the untripped configuration fell in the middle of the data for the tripped configuration. Therefore, it appeared that no significant difference in spanwise uniformity existed between the tripped and untripped configurations in the wake.

#### IV. Summary and Concluding Remarks

New, higher-resolution measurements were obtained as part of an extended experimental campaign to investigate the unsteady wake interference between a pair of circular cylinders in tandem arrangement. The goal behind the work reported herein was to significantly expand the previously acquired experimental database, which is generically relevant to the studies of unsteady flow and noise generation for landing gear systems. By rotationally “clocking” the cylinders, data were obtained at higher circumferential resolution for RMS surface pressure fluctuations, revealing finer details of the unsteady pressure field. Such details revealed areas of wake interaction on the rear cylinder that yielded higher levels of RMS pressure fluctuations. Higher-resolution PIV data revealed the meandering nature of the separated shear layers from the cylinders and the resulting unsteady interactions with the rear cylinder surface, possibly producing the broadband, humplike features in the unsteady pressure spectra obtained during previous studies.

The changes in flow characteristics from subcritical to supercritical range of cylinder spacings were investigated in detail and a rapid increase in pressure drag was noted to occur near  $L/D = 3.0375$ , accompanied by a small overshoot in drag for cylinder spacing between 3 and 3.4 diameters. Instantaneous PIV results showed that two distinct flow modes were in evidence at the critical spacing ( $L/D = 3.0375$ ), with a random, intermittent switching between the two modes. One of the two modes from this bistable state flow behavior was similar to the flow at lower, subcritical spacings, in that it showed no roll-up of the shear layers separating from the front cylinder, but a consistent reattachment along the rear cylinder. The other mode revealed robust shedding of vortices due to

alternate roll-up of the shear layers from the top and bottom surfaces of the front cylinder. Due to an intermittent switching between these two modes, the pressure signals near the reattachment location along the rear cylinder showed similarly intermittent amplitude attenuation at the same intervals when the short-time Fourier transforms indicated a loss of tonal peaks in the frequency spectra. Probability density function (PDF) estimates for the fluctuating surface pressure within the bistable state reflected a superposition of the PDFs corresponding to the shedding and non-shedding modes, respectively. The substantially higher spanwise correlation distances that occur during the bi-stable state, accompanied by a relatively modest decrease in fluctuating pressure levels relative to those at larger cylinder spacings, indicate the possibility of stronger acoustic radiation at near-critical cylinder spacing. The experimental measurements of the bistable state behavior are particularly important because of the challenges in computing such intermittent flows, which are compounded by the need for substantially longer integration times for the numerical simulation.

The effect of boundary layer tripping along the rear cylinder was investigated for both subcritical ( $L/D = 1.435$ ) and supercritical ( $L/D = 3.7$ ) spacings. Whereas the rear cylinder trip has a negligible impact on the measured flow behavior on both cylinders at  $L/D = 1.435$ , a noticeable effect was found on the rear cylinder at  $L/D = 3.7$ , despite the anticipated, trip-like effect of turbulent wake impingement from the upstream cylinder. The effect of boundary layer tripping on the rear cylinder was manifested in multiple ways, namely, reduced peaks in mean  $C_p$  distribution along the rear cylinder, accompanied by an earlier separation from the cylinder surface, a reduced pressure recovery, and a correspondingly higher drag; lower levels of mean TKE in the wake of the rear cylinder compared to the untripped case; and reduced levels of peak surface pressure fluctuations over the rear cylinder. The above trends suggest that the untripped boundary-layer flow upstream of separation along the rear cylinder was transitional but not fully turbulent in character.

We note that, because of the complexity of component interactions within a landing gear flow field, the present tandem cylinder dataset will not be directly applicable to the prediction of undercarriage noise. However, it provides a glimpse into the range of expected flow patterns over an actual undercarriage and, hence, a useful means to validate computational tools, interpret the limited measurements on more complex configurations, and to guide the development of noise prediction models with reduced empiricism.

### Acknowledgments

The authors express their appreciation to Mr. Donald Day for his assistance with the experimental setup, instrumentation, and data acquisition; Mr. Jerome Harris for optical setup and assisting with data acquisition during the PIV measurements and Dr. Chung-Sheng Yao for advice on the PIV measurements; Mr. Tom Hall and Mr. Mick Hartzheim for installation and wiring of the pressure transducers; and to Mr. Floyd Backley and Mr. Tim Wood for the model design and fabrication. M.C. Author also acknowledges useful technical discussions with Dr. Craig Streett during the conceptual design of the model.

### References

- <sup>1</sup> Stoker, R., Guo, Y., Streett, C., and Burnside, N., "Airframe Noise Source Locations of a 777 Aircraft in Flight and Comparisons with Past Model Tests," AIAA Paper 2003-3232, May, 2003.
- <sup>2</sup> Jenkins, L. N., Khorrami, M. R., Choudhari, M. M., and McGinley, C. B., "Characterization Of Unsteady Flow Structures Around Tandem Cylinders For Component Interaction Studies In Airframe Noise," AIAA-2005-2812, 2005.
- <sup>3</sup> Jenkins, L. N., Neuhart, D. H., McGinley, C. B., Choudhari, M. M., and Khorrami, M. R., "Measurements Of Unsteady Wake Interference Between Tandem Cylinders," AIAA-2006-3202, 2006.
- <sup>4</sup> Hutcheson, F. V. and Brooks, T. F., "Noise radiation from Single and Multiple Rod Configurations," AIAA-2006-2629, 2006.
- <sup>5</sup> Lockard, D. P., Khorrami, M. R., Choudhari, M. M., Hutcheson, F. V., and Brooks, T. F., "Tandem Cylinder Noise Predictions," AIAA-2007-3450, 2007.
- <sup>6</sup> Lockard, D. P., Choudhari, M. M., Khorrami, M. R., Neuhart, D. H., Hutcheson, F. V., and Brooks, T. F., "Aeroacoustic Simulations of Tandem Cylinders with Subcritical Spacing," AIAA-2008-2862, 2008.
- <sup>7</sup> Khorrami, M. R., Choudhari, M. M., Lockard, D. P., Jenkins, L. N. and McGinley, C. B., "Unsteady Flowfield Around Tandem Cylinders as Prototype for Component Interaction in Airframe Noise," AIAA Journal, Vol. 45, No. 8, 2007, pp. 1930-1941.
- <sup>8</sup> Khorrami, M. R., Lockard, D. P., Choudhari, M. M., Jenkins, L. N., Neuhart, D. H., and McGinley, C. B., "Simulations of Bluff Body Flow Interaction for Noise Source Modeling," AIAA 2006-3203, 2006.

- <sup>9</sup>Zdravkovich, M.M., “Flow Induced Oscillations of Two Interfering Circular Cylinders,” *J. of Sound and Vibrations*, Vol. 101, No.4, 1985, pp. 511-521.
- <sup>10</sup>Sellers, W. L. and Kjelgaard, S. O., “The Basic Aerodynamic Research Tunnel – A Facility Dedicated to Code Validation,” AIAA-88-1997, May 1988.
- <sup>11</sup>Jenkins, L. N., “An Experimental Investigation of the Flow over a Notchback Automobile Configuration,” Master of Science Thesis, George Washington University, 1999.
- <sup>12</sup>Roshko, A. “Experiments on the Flow Past a Circular Cylinder At Very High Reynolds Number,” *Journal of Fluid Mechanics*, Vol. 10, 1961, pp 345-356.
- <sup>13</sup>Ljungkrona, L, Norberg, C., and Sunden, B., “Free-stream Turbulence and Tube Spacing Effects on Surface Pressure Fluctuations for Two Tubes in an In-line Arrangement,” *Journal of Fluids and Structures*, Vol. 5, 1991, pp. 701-727.
- <sup>14</sup>Okajima, A., “Flow Around Two Tandem Circular Cylinders at Very High Reynolds Numbers,” Bulletin of the JSME, Vol. 22, No. 166, April 1976, pp. 504-511.
- <sup>15</sup>Igarashi, T., “Characteristics of Flow Around Two Circular Cylinders Arranged in Tandem,” Bulletin of the JSME, Vol. 24, No. 188, February 1981, pp. 323-331.
- <sup>16</sup>Ohya, Y., Okajima, A., and Hayashi, M., “Wake Interference and Vortex Shedding,” Encyclopedia of Fluid Mechanics, edited by N.P. Chermisinoff (Gulf Publishing Company, Houston), Vol. 8, 1989, pp.323-389.
- <sup>17</sup>Zdravkovich, M.M., Pridden, D. L., “Interference Between Two Circular Cylinders; Series of Unexpected Discontinuities,” *Journal of Wind Engineering and Industrial Aerodynamics*, 2, 1977, pp. 255-270.
- <sup>18</sup>Bendat, Julius S.; Piersol, Allan G.: *Random Data: Analysis and Measurement Procedures*. John Wiley & Sons, 2000.
- <sup>19</sup>Mitra, Sanjit K.: *Digital Signal Processing: A Computer-Based Approach*. McGraw-Hill, 1998.
- <sup>20</sup>Arie, M., Kiya, M., Moriya, M., and Mori, H., “Pressure Fluctuations on the Surface of Two Circular Cylinders in Tandem Arrangement,” *J. Fluids Engineering*, Vol. 105, June 1983, pp. 161-167.
- <sup>21</sup>Bruun, H.H, and Davies, P.O.A.L., “An Experimental Investigation of the Unsteady Pressure Forces on a Circular Cylinder in a Turbulent Cross Flow,” *J. of Sound and Vibration*, Vol. 40, No.4, pp. 535-559, 1975.

**Table 1. Estimated Experimental Uncertainties**

Steady Cp	0.02
Drag Coefficient	0.0005
PIV: Umean, Vmean	0.03 (normalized)
PIV: Spanwise Vorticity	1.8 (normalized)
PIV: TKE	4%
Power Spectral Density (PSD)	10-20%
Cp'rms	5-11%
Rpp	2-6%
Lcorr/D	3-7%
Probability Density Function (PDF)	0.003-0.005
Diameter, D; Sensor spacing, Δz	0.005"

**Table 2. 2-D PIV Specifications**

Light sheet thickness	2 mm
Lasers	Dual 220 mJ, Nd-YAG
Digital camera frame rate	5 Hz
Sensor size	1360x1036 pixels
Measurement volume (50 mm lens, 24X24 pixel interrogation window)	1.0 X 1.0 mm
Measurement volume (105 mm lens, 30X30 pixel interrogation window)	0.649X 0.649 mm
Interrogation window overlap	50%
Flow seeding technique	Commercial fog generator
Image pairs per configuration	1500

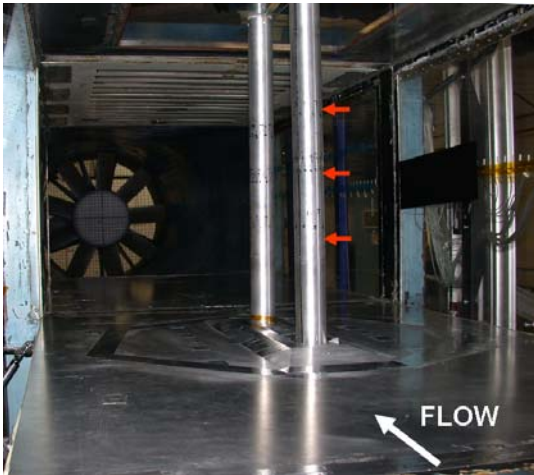


Figure 1. Tandem cylinder configuration in the BART facility.

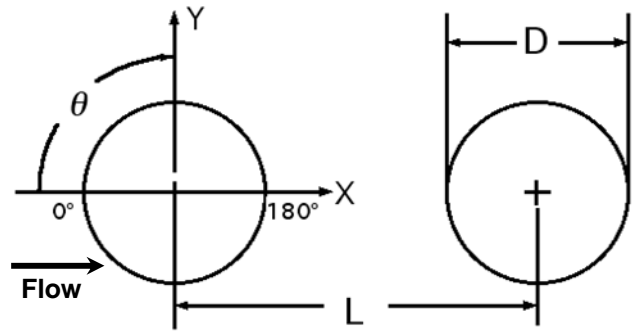


Figure 2. Model schematic and coordinate reference system.

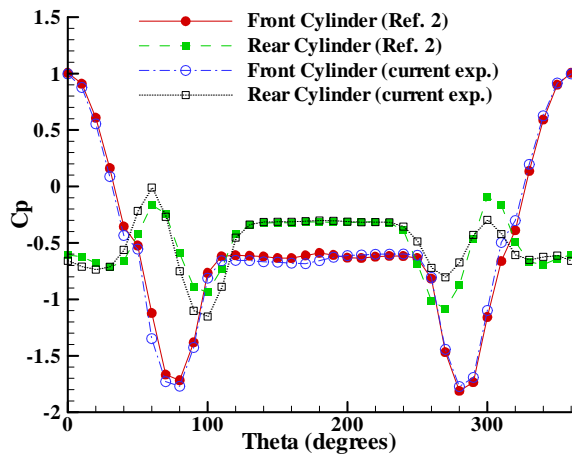


Figure 3. Pressure distribution comparison between previous and current tunnel entries,  $L/D=1.435$ ,  $D=2.25''$  (Boundary layer along front cylinder tripped between  $50^\circ - 60^\circ$  and  $300^\circ - 310^\circ$ , respectively.).

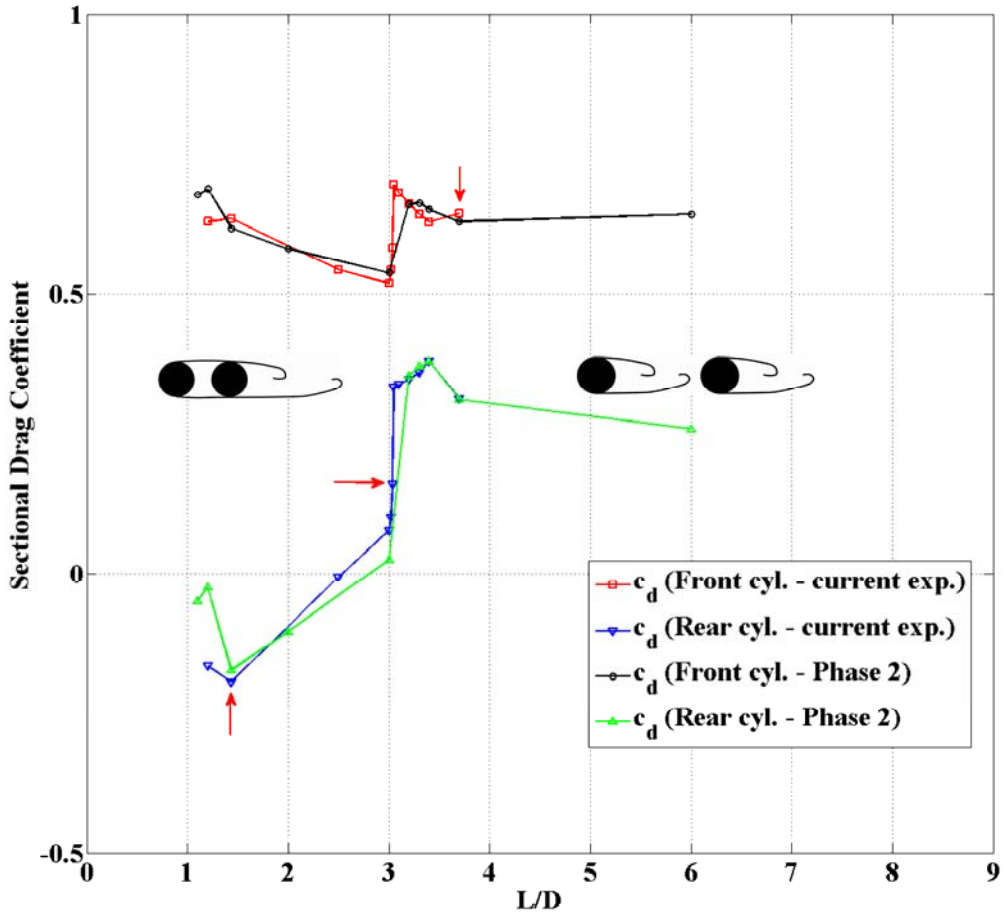


Figure 4. Effect of cylinder spacing on sectional drag coefficient. Arrows indicate the cylinder spacings of primary interest in this paper, namely,  $L/D = 1.435$  (subcritical spacing),  $3.0375$  (critical spacing), and  $3.7$  (supercritical spacing), respectively (Phase 2 in legend from Ref. 2).

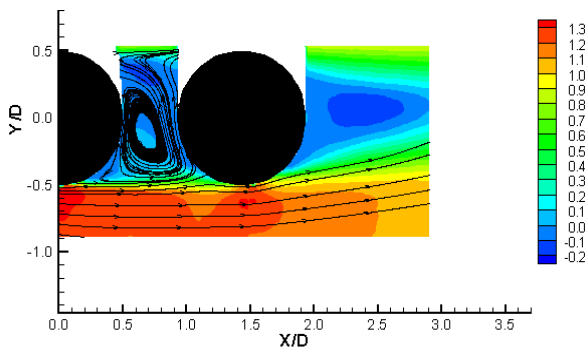


Figure 5a. Mean streamlines in gap region ( $L/D = 1.435$ ) – previous test,  $D=1.75''$ .

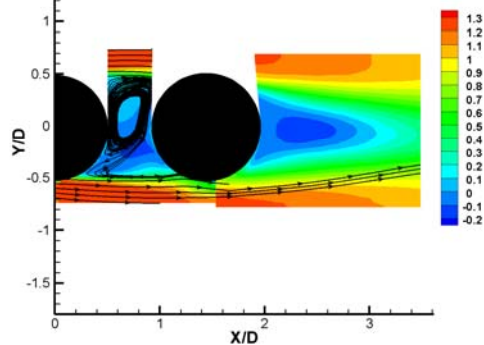


Figure 5b. Mean streamlines in gap region ( $L/D = 1.435$ ) – current experiment,  $D=2.25''$ .

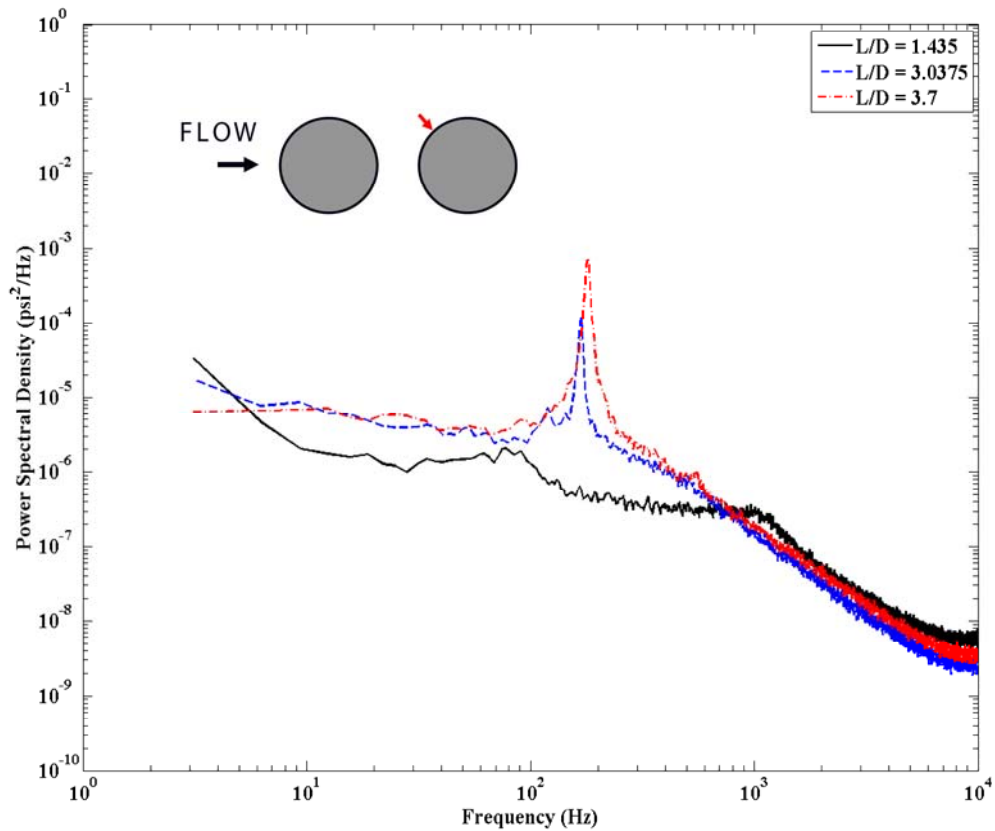


Figure 6. Power spectral density of unsteady pressure at  $\theta = 45^\circ$ , rear cylinder. Red arrow along the rear cylinder indicates the sensor location.

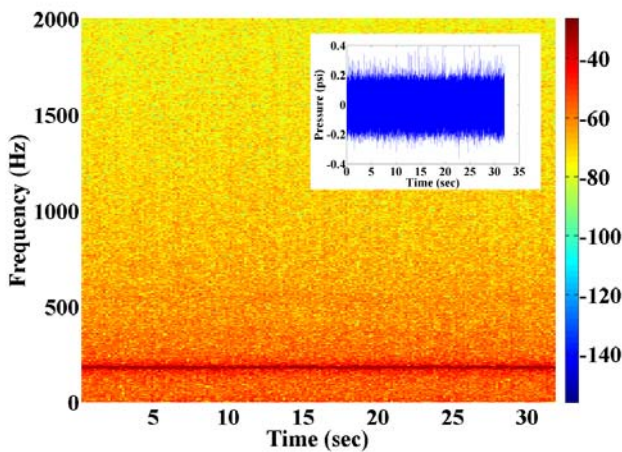


Figure 7a. Spectrogram at  $\theta = 45^\circ$ , rear cylinder ( $L/D = 3.7$ ), colors are levels of  $10 \cdot \log_{10}(\text{abs}(G_{p'p'}))$ .

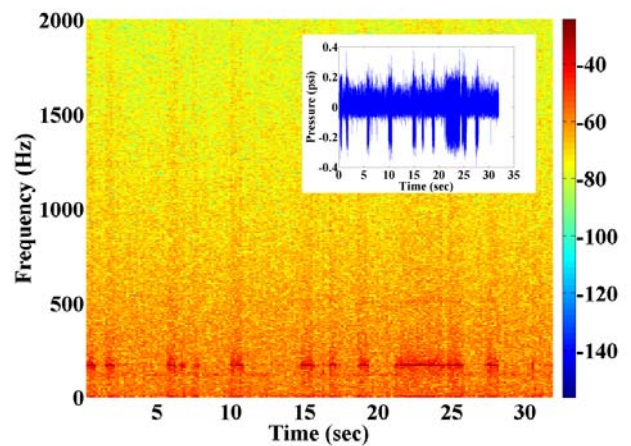


Figure 7b. Spectrogram at  $\theta = 45^\circ$ , rear cylinder ( $L/D = 3.0375$ ), colors are levels of  $10 \cdot \log_{10}(\text{abs}(G_{p'p'}))$ .

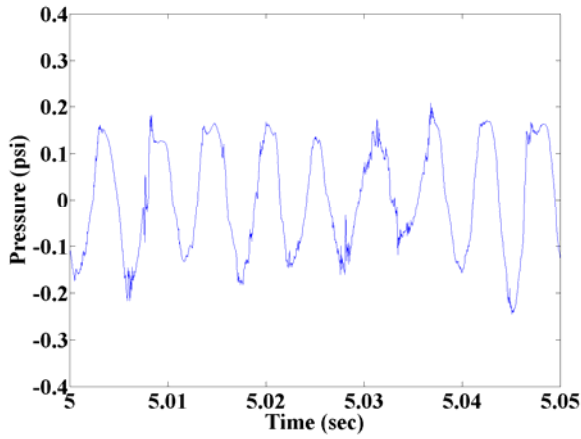


Figure 7c. Expanded time series of pressure signal,  $L/D=3.7$ .

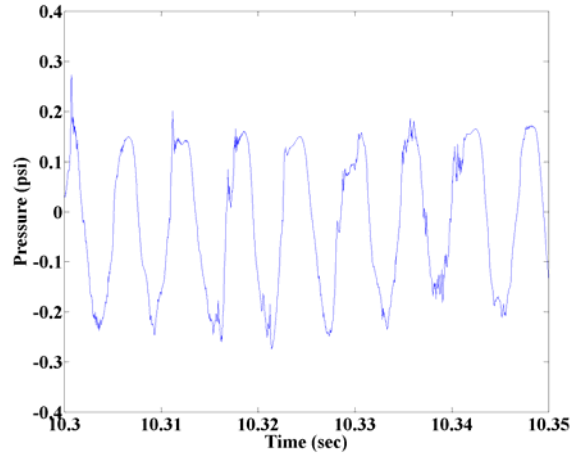


Figure 7d. Expanded time series of pressure signal, periodic (i.e., vortex shedding) mode at  $L/D=3.0375$ .

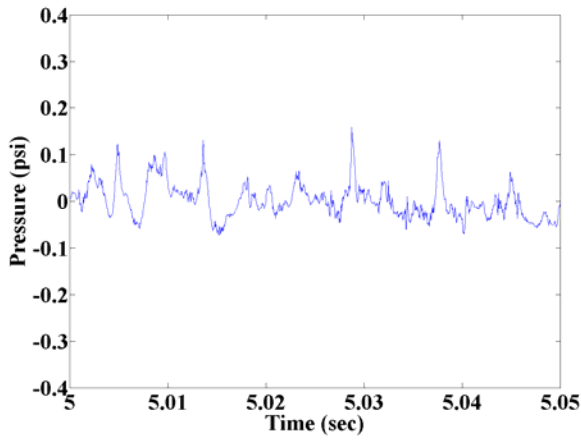


Figure 7e. Expanded time series of pressure signal, aperiodic (i.e., non-shedding) state at  $L/D=3.0375$ .

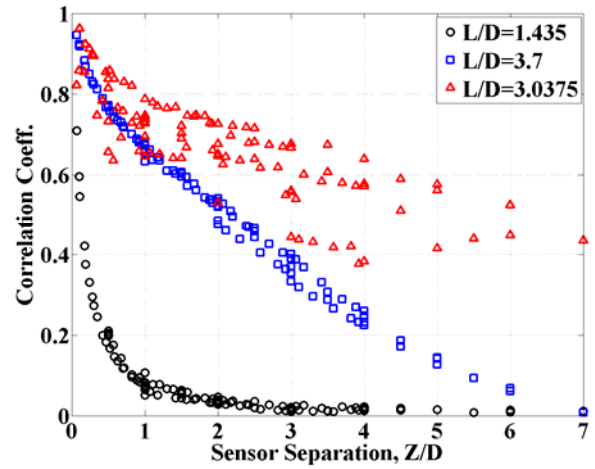


Figure 8a. Longitudinal pressure correlation as a function of transducer spacing. Sensors at  $\theta = 135^\circ$ , rear cylinder.

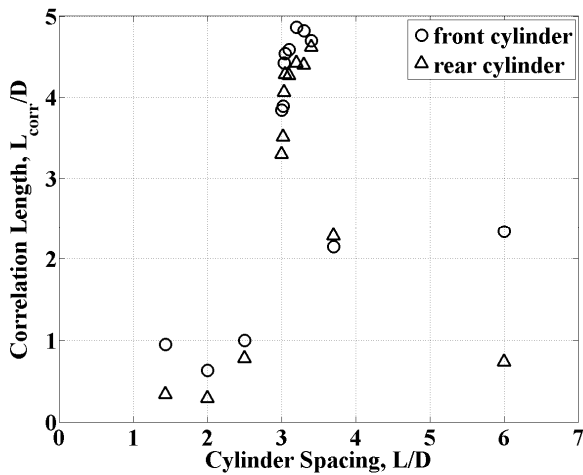


Figure 8b. Longitudinal correlation length as function of cylinder spacing. Sensors at  $\theta = 135^\circ$  along both cylinders.

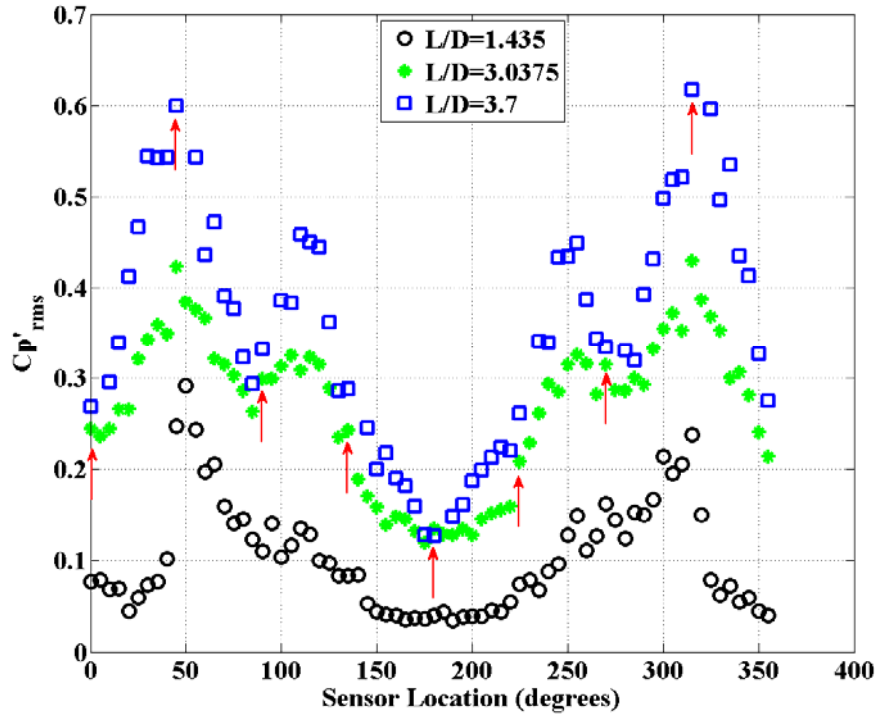


Figure 9. RMS pressure coefficients on rear cylinder (red arrows indicate non-clocked transducer locations).

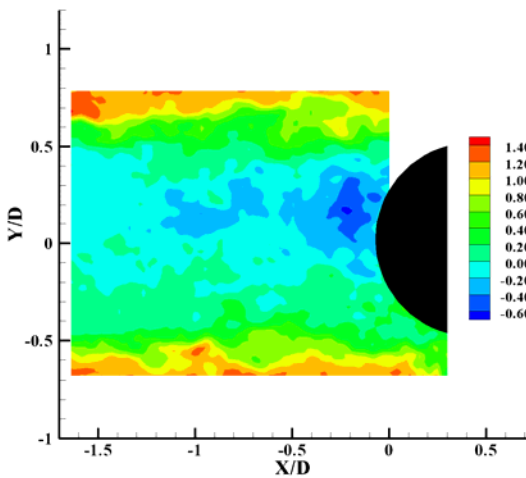


Figure 10a. Instantaneous streamwise velocity ahead of rear cylinder,  $L/D=3.0375$

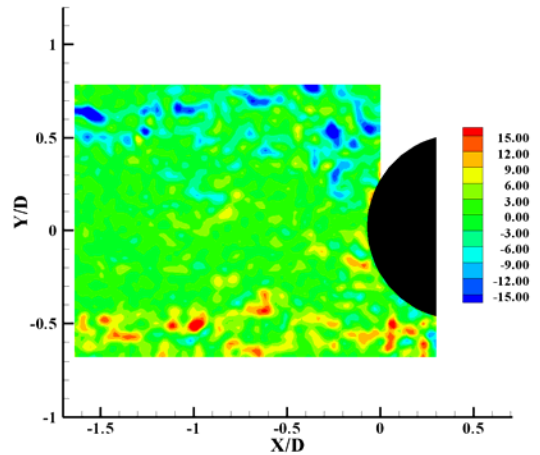


Figure 10b. Instantaneous spanwise vorticity corresponding to velocity field in Fig. 11a.

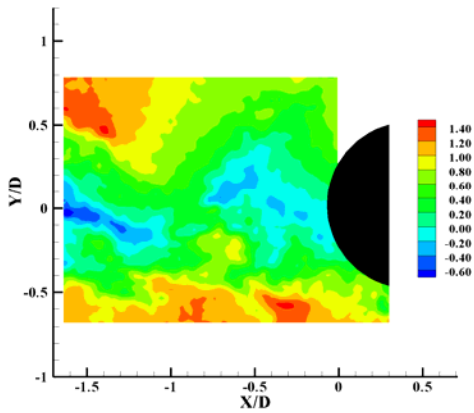


Figure 11a. Instantaneous streamwise velocity ahead of rear cylinder,  $L/D=3.0375$

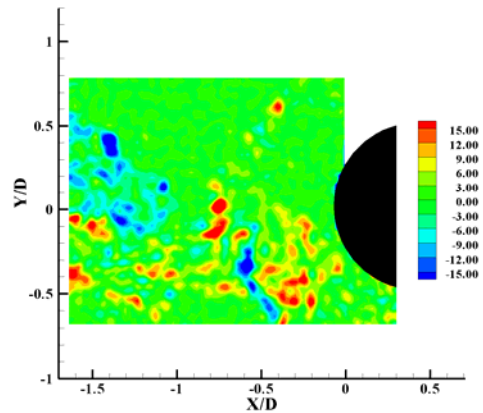
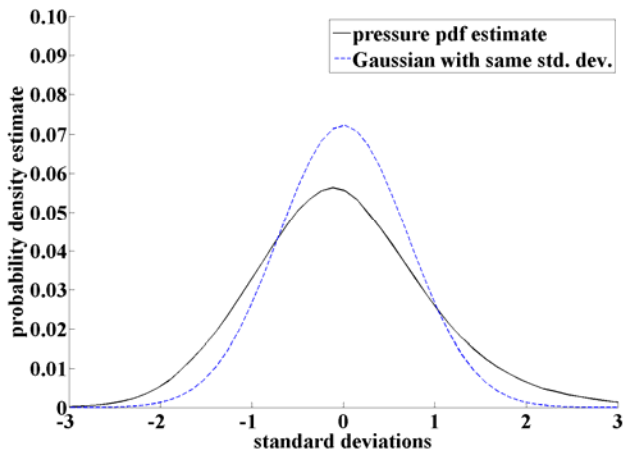
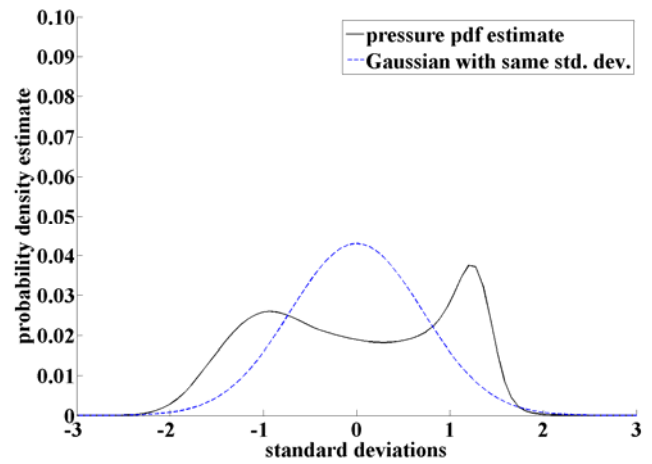


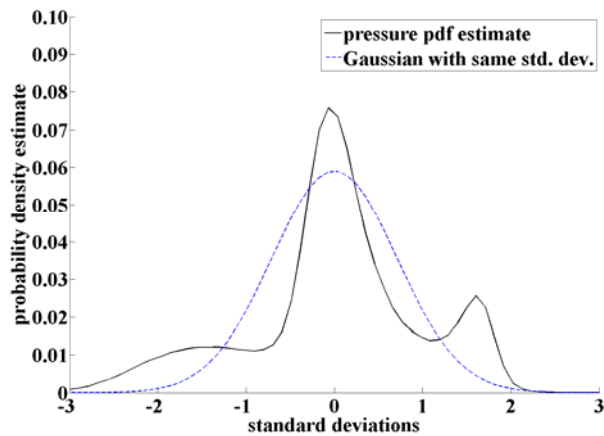
Figure 11b. Instantaneous spanwise vorticity corresponding to velocity field in Fig. 11a.



12a)  $L/D=1.435$



12b)  $L/D=3.7$



12c)  $L/D=3.0375$

Figure 12. Probability density estimates of pressure at 45-degree azimuthal location along rear cylinder.

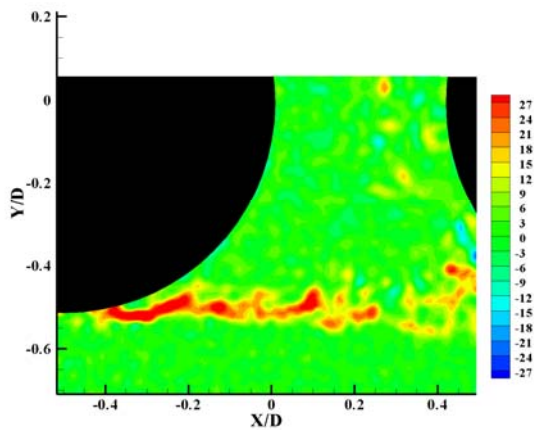


Figure 13a. Instantaneous spanwise vorticity within gap region,  $L/D=1.435$ .

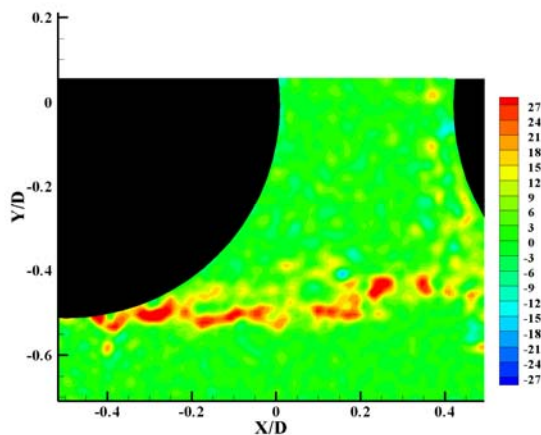


Figure 13b. Instantaneous spanwise vorticity within gap region,  $L/D=1.435$ .

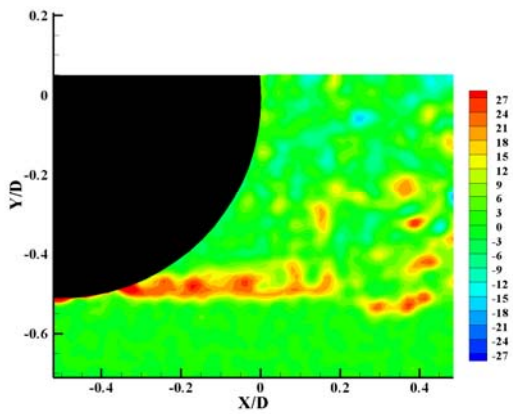


Figure 14a. Instantaneous spanwise vorticity behind front cylinder,  $L/D=3.7$ .

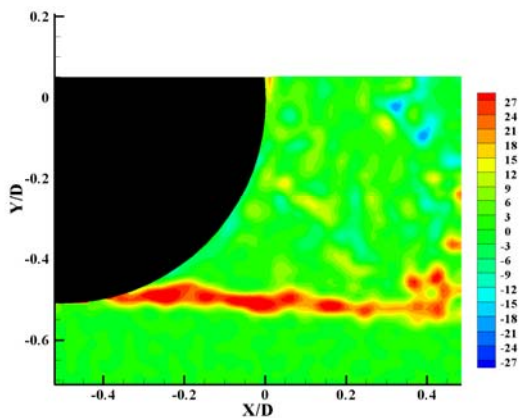


Figure 14b. Instantaneous spanwise vorticity behind front cylinder,  $L/D=3.7$ .

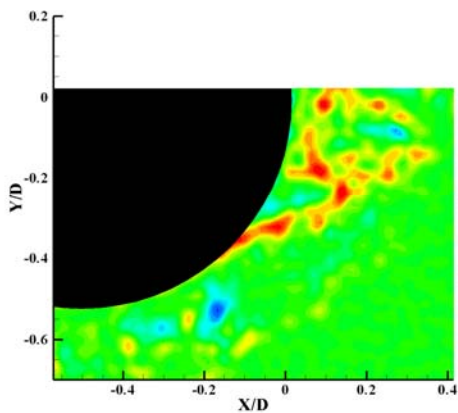


Figure 15a. Instantaneous spanwise vorticity behind rear cylinder,  $L/D=3.7$ .

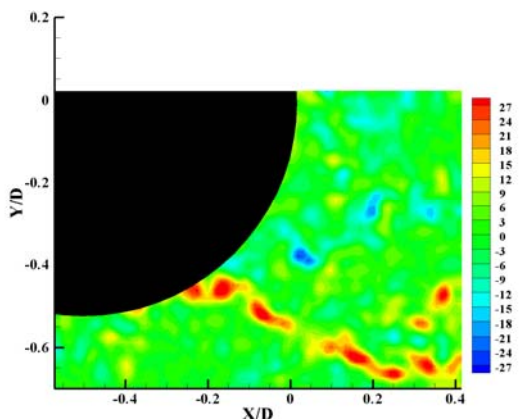


Figure 15b. Instantaneous spanwise vorticity behind rear cylinder,  $L/D=3.7$ .

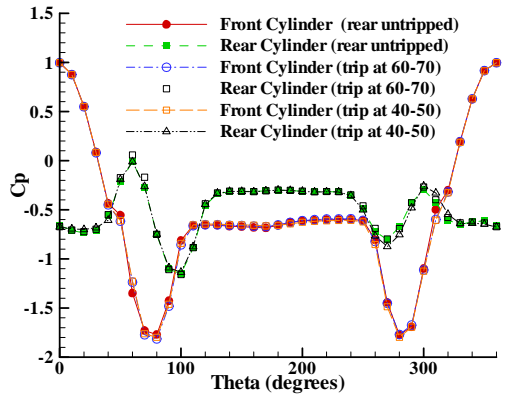


Figure 16a.  $L/D=1.435$ .

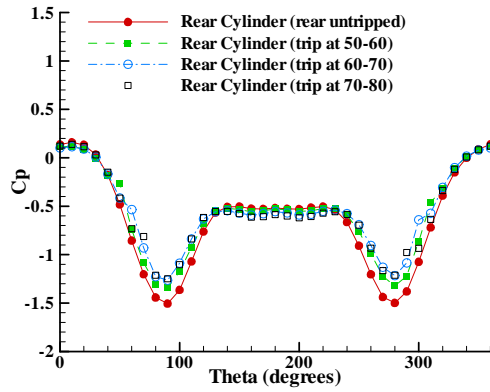


Figure 16b.  $L/D=3.7$ .

Figure 16. Mean surface pressure distribution, effect of boundary layer trip on rear cylinder

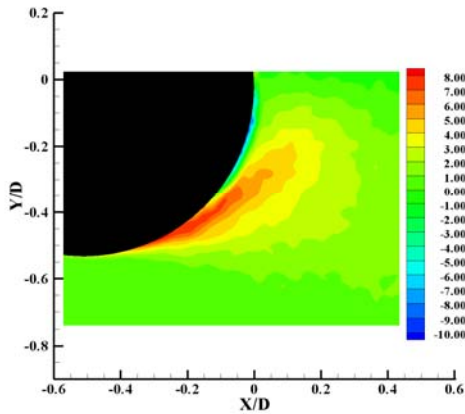


Figure 17a. No trip on rear cylinder.

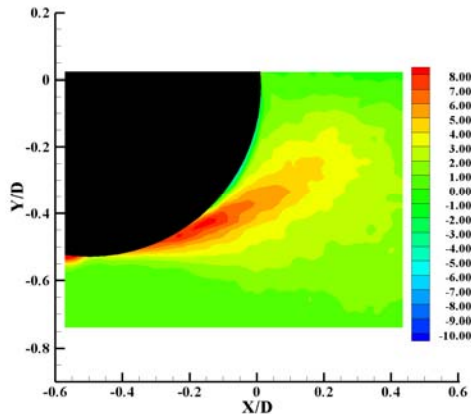


Figure 17b. With trip on rear cylinder.

Figure 17. Effect of boundary layer trip along rear cylinder on mean spanwise vorticity behind the cylinder ( $L/D=3.7$ )

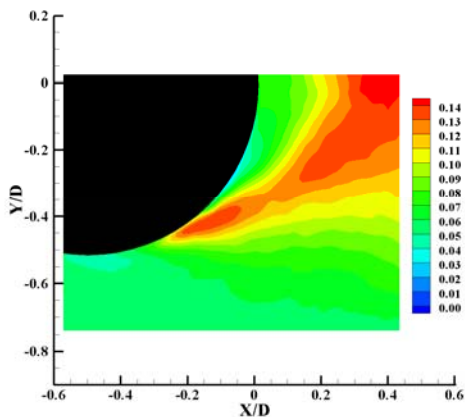


Figure 18a. No trip on rear cylinder.

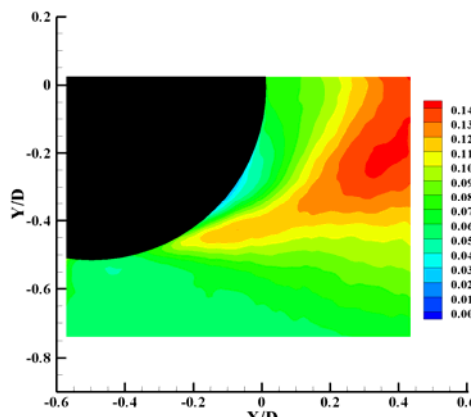


Figure 18b. With trip on rear cylinder.

Figure 18. Effect of boundary layer trip along rear cylinder on mean TKE behind the cylinder ( $L/D=3.7$ )

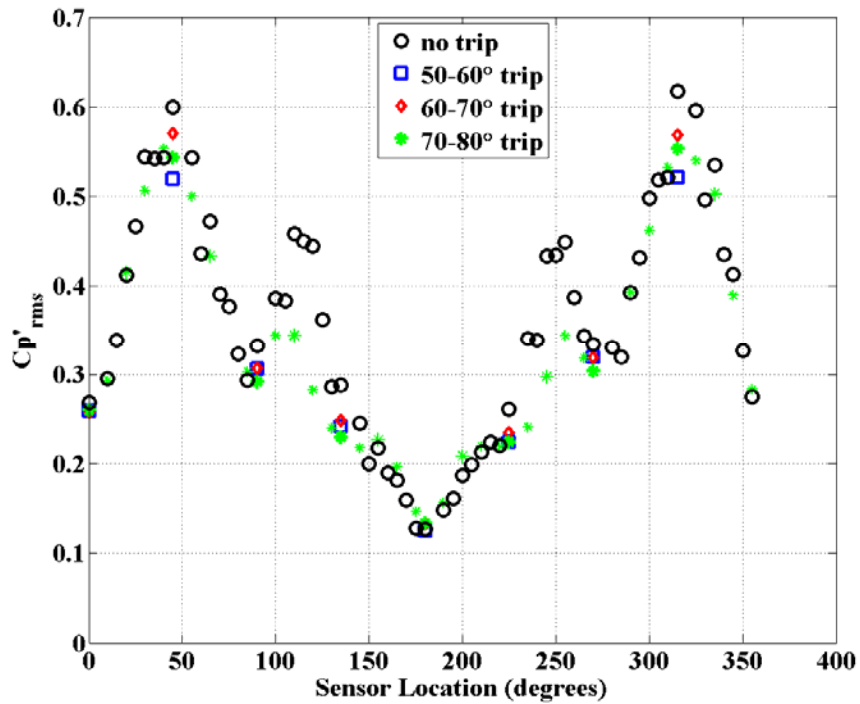


Figure 19. Effect of rear cylinder trip on RMS pressure coefficients on rear cylinder,  $L/D=3.7$ .

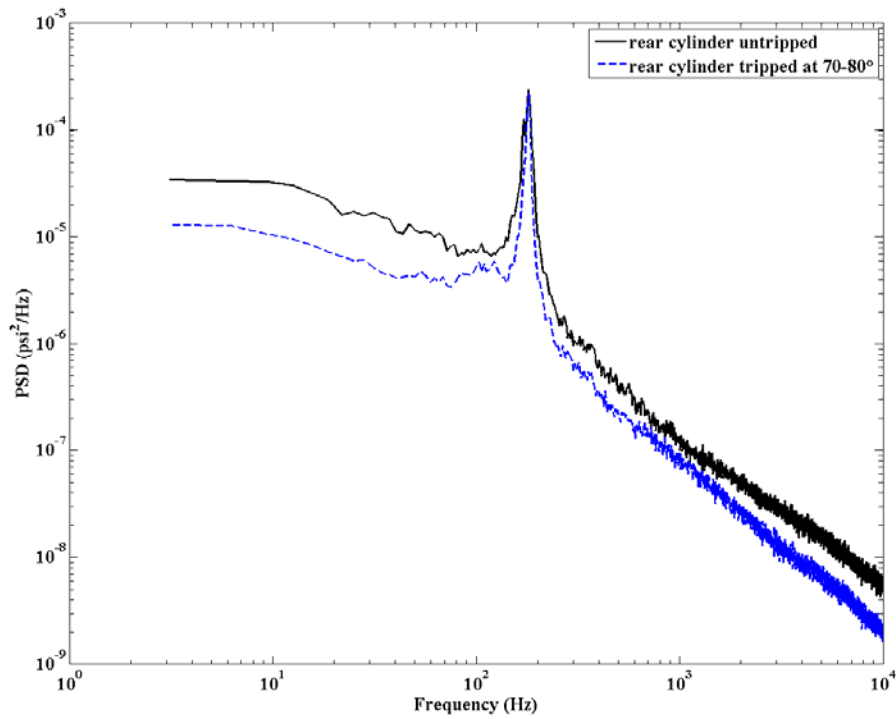


Figure 20. Power spectral density of unsteady pressure at  $\theta = 110^\circ$ , rear cylinder,  $L/D=3.7$ .